Journal of the Optical Society of America A
OPTICS, IMAGE SCIENCE, AND VISION

Adaptive Bayesian augmented Lagrangian algorithm for fluorescence molecular tomography

Bianbian Yang,[1] Yiting He,[1] Nannan Cai,[1] Jun Zhang,[1] Yi Chen,[1,2,4] Yangyang Liu,[1,5] Chengyi Gao,[3] Huangjian Yi,[1] and Xin Cao[1,6]

[1]School of Information Science and Technology, Northwest University, Xi'an, Shaanxi 710127, China
[2]School of Electrical and Mechanical Engineering, The University of Adelaide, Adelaide, SA 5005, Australia
[3]Department of Oncology, The First Affiliated Hospital, Xi'an Jiaotong University, Xi'an, Shaanxi 710061, China
[4]yichen.cgz@gmail.com
[5]yyliu@nwu.edu.cn
[6]caoxin918@hotmail.com

Received 17 September 2025; revised 29 November 2025; accepted 7 December 2025; posted 9 December 2025; published 24 December 2025

Fluorescence molecular tomography (FMT) is a noninvasive imaging technique that enables the quantitative three-dimensional reconstruction of fluorescent probe distributions *in vivo*. However, FMT reconstruction is limited in accuracy and reliability due to light scattering and the ill-posed inverse problem. In this paper, the adaptive Bayesian augmented Lagrangian (ABAL) algorithm is proposed, which adaptively adjusts the regularization parameter to promote sparsity and enhance robustness to noise, while significantly improving computational efficiency. By integrating sparse Bayesian learning (SBL) with the augmented Lagrangian (AL) framework, the approach addresses the computational challenges and non-convexity introduced by the iterative adjustment of regularization parameters in SBL. The inverse problem is reformulated as a weighted L_1 minimization with adaptive regularization and solved via the AL method, enhancing computational efficiency and mitigating the risk of local minima. Moreover, the adaptive regularization mechanism enables the method to dynamically adjust to data-specific characteristics, avoiding over-regularization or under-regularization and improving both stability and reconstruction accuracy. To evaluate the effectiveness of our method, a series of numerical simulations and implantation experiments were conducted. Results confirm that the ABAL method can achieve relatively accurate reconstruction performance compared to other approaches, with an average minimum localization error (LE) of 0.358 mm and an average Dice coefficient of 0.775. These results show relatively high localization accuracy, shape recovery, and robustness of the ABAL method in FMT reconstruction, indicating its potential for practical FMT application.

https://doi.org/10.1364/JOSAA.579369

1. INTRODUCTION

Fluorescence molecular tomography (FMT) is a noninvasive optical imaging modality for reconstructing the three-dimensional distribution of fluorescent probes *in vivo* [1,2]. Upon external light excitation, targeted fluorophores emit fluorescence signals that are subsequently detected at the tissue surface [3]. FMT reconstruction is based on a photon propagation model, typically approximated by the diffusion equation derived from the radiative transfer equation [4,5]. FMT has been increasingly adopted in recent years for preclinical research and small animal imaging owing to its moderate imaging depth, high sensitivity, and quantitative capability [6]. It is valuable in applications such as early disease detection, drug delivery evaluation, and tumor molecular characterization, highlighting its growing importance in biomedical imaging [7,8]. However, the inverse problem is severely ill-posed due to complex tissue scattering and absorption, making FMT reconstruction highly sensitive to noise and numerical instability [9,10].

To address the ill-posed inverse problem in FMT reconstruction, various methodological frameworks have been proposed [11]. Among them, regularization-based methods incorporate structural priors as penalty terms in the optimization objective to stabilize the solution [12]. Classical regularization strategies include L_2-norm regularization [13] and L_1-norm regularization [14]. While L_2-norm regularization enhances robustness and stabilizes the inverse solution by penalizing large deviations, it often results in overly smooth reconstructions that obscure fine structural details [15,16]. In contrast, L_1-norm regularization promotes sparsity in the fluorescence source distribution and helps preserve sharp features but is sensitive to noise and the measurement matrix conditioning [17]. Beyond convex regularization approaches, non-convex sparse regularization

(NSR) methods, such as smoothly clipped absolute deviation (SCAD) [18] and minimax concave penalty (MCP) [19], have been explored to strike a better balance between sparsity and stability [20]. While these methods preserve structural features and achieve higher reconstruction accuracy by balancing data fidelity and sparsity constraints, they increase computational complexity due to non-convex optimization, posing challenges in convergence and algorithmic robustness [21]. To further enhance reconstruction accuracy and better capture the sparse structure of fluorescence distributions, dictionary learning techniques have been introduced. It typically involves two alternating stages: sparse coding and dictionary update. Sparse coding computes sparse representations using a fixed dictionary, while dictionary update adjusts the dictionary to better fit the data [22]. For instance, the ROMP-DCP method [23] implements this strategy through regularized orthogonal matching pursuit (ROMP) for sparse coding and difference of convex (DC) programming for dictionary updates. This alternating optimization enables the model to leverage data-adaptive representations, improving reconstruction sparsity and accuracy [23]. However, dictionary learning methods lack an adaptive mechanism to automatically determine sparsity levels from the observed data, which may restrict its generalizability and robustness [23].

To overcome these limitations, Bayesian frameworks reformulate the inverse problem as a probabilistic inference [24]. Unlike regularization-based methods that rely on fixed penalties, Bayesian approaches model the fluorescence distribution as a random variable with prior distributions, allowing uncertainty quantification and flexible incorporation of structural priors such as expected sparsity or spatial smoothness [25,26]. They also adapt the regularization strength and sparsity level to the observed data, mitigating the lack of adaptability in dictionary learning methods and enhancing robustness across varying imaging conditions [27]. For example, sparse Bayesian learning (SBL) promotes sparsity by assigning hierarchical priors to solution coefficients, which are iteratively updated to adapt to varying imaging conditions [28]. Gaussian Markov random fields (GMRFs) capture spatial correlations in biological tissues by enforcing local smoothness [24]. However, Bayesian inference often relies on computationally intensive techniques such as Markov chain Monte Carlo (MCMC) sampling or variational inference [29,30]. In high-dimensional FMT problems, these methods become computationally expensive, necessitating innovations to improve scalability without compromising reconstruction accuracy [30].

To address these challenges, an adaptive Bayesian augmented Lagrangian (ABAL) algorithm is proposed for FMT reconstruction. ABAL combines the sparsity-promoting power of SBL with the computational efficiency of the augmented Lagrangian (AL) optimization strategy. The ill-posed inverse problem is reformulated as a weighted L_1 minimization, where SBL introduces hierarchical sparsity priors and adaptively adjusts regularization strength based on the posterior distribution. This adaptivity allows the algorithm to vary noise levels and data characteristics, eliminating the need for manual tuning. Meanwhile, the AL method decomposes the resulting non-convex problem into manageable convex sub-problems, solved iteratively by alternating updates of auxiliary variables and Lagrange multipliers, accelerating convergence and numerical stability. We comprehensively evaluate the ABAL algorithm through a series of numerical simulations and implantation experiments, comparing it with three algorithms: the fast iterative shrinkage thresholding algorithm (FISTA) based on L_1-norm [31], the incomplete variables truncated conjugate gradient (IVTCG) based on L_1-norm [32], and the orthogonal matching pursuit (OMP) based on L_0-norm [33].

The remainder of this paper is organized as follows. Section 2 introduces the FMT reconstruction model and the ABAL algorithm. Section 3 presents the evaluation metrics and experimental design. Section 4 provides 3D visualization results and quantitative performance analysis. Finally, Section 5 summarizes the major contributions of this study and discusses future work.

2. METHODOLOGY

A. Photon Propagation Model

In steady-state FMT with point excitation sources, photon propagation in biological tissues, which exhibit high scattering and low absorption in the near-infrared spectral range, can be approximated by the diffusion equation (DE) [34,35]. To accurately simulate photon behavior at tissue boundaries, DE is coupled with Robin boundary conditions that account for partial reflection and transmission of photons at the interface between tissue and the external medium [36,37], which are defined as follows:

$$\begin{cases} -\nabla \cdot (D_x(r)\nabla\Phi_x(r)) + \mu_{ax}(r)\Phi_x(r) = \Theta\delta\,(r - r_s) \\ -\nabla \cdot (D_m(r)\nabla\Phi_m(r)) + \mu_{am}(r)\Phi_m(r) = \Phi_x(r)\eta\mu_{af}(r) \end{cases} \quad r \in \Omega, \tag{1}$$

where r denotes the position vector within the imaging domain Ω, and r_s refers to the location vector of the point excitation sources. The diffusion and absorption coefficients for excitation and emission light are denoted as D_x, μ_{ax} and D_m, μ_{am}, respectively. The photon flux densities at position r for excitation and emission light are $\Phi_x(r)$ and $\Phi_m(r)$, respectively. The fluorescence source to be reconstructed is represented by μ_{af}.

By applying the finite-element method (FEM) [38], the continuous photon propagation model described by the partial differential Eq. (1) is discretized over the computational domain, which is converted into the following linear algebraic equation:

$$AX = \Phi, \tag{2}$$

where A is a $m \times n$ forward system matrix, which contains the specific optical property information of each part of the organism. The light intensity density on the surface of the organism Φ can be obtained by practical measurement, and it is a column vector of $m \times 1$ dimension, and X is the distribution of the fluorescent source to be reconstructed within the biological tissue.

B. ABAL Method for FMT Reconstruction

The ABAL method comprises two principal stages. First, the SBL model reformulates the ill-posed inverse problem as a weighted L_1 minimization problem to enhance sparsity adaptability. Second, the weighted problem is solved under the AL framework utilizing Lagrange multipliers and an alternating iterative strategy for efficient computation.

Specifically, the first stage uses the SBL model to incorporate sparsity priors via Bayesian inference, casting FMT reconstruction as a weighted L_1 minimization problem. To address the ill-posed property of FMT, SBL iteratively updates the weights, dynamically adjusting regularization parameters to varying imaging conditions. This strategy promotes optimal sparsity in reconstructed solutions while avoiding the over-sparsification seen in traditional L_1 methods. In the second stage, the weighted problem is solved within the AL framework by introducing Lagrange multipliers and decomposing it into smaller and more tractable sub-problems [39]. These sub-problems are efficiently solved using an alternating iterative scheme, which accelerates convergence and reduces computational complexity while maintaining high reconstruction accuracy.

1. Weighted L_1 Minimization Problem

Considering background noise and data acquisition errors in FMT, Eq. (3) can be reformulated as

$$AX + \xi = \Phi, \tag{3}$$

where ξ represents the combined effect of background noise and measurement error.

SBL is formulated as an iterative weighted L_1 regularization method based on a Bayesian probabilistic framework, where model parameters are treated as random variables with assigned priors [39]. Given the parameter X, the likelihood function of the observed data Φ in Eq. (3) is

$$P(\Phi|X) = \mathcal{N}(\Phi|AX, \lambda I) \propto \exp\left[-\frac{1}{2\lambda}||AX - \Phi||_2^2\right], \tag{4}$$

where λ denotes the variance of the observation noise. In Bayesian inference, the prior distributions with heavy-tailed characteristics are typically employed to effectively capture the sparsity of the unknown parameters. The assumed prior distribution of $P(X)$ is given as follows:

$$P(X) \propto \exp\left[-\frac{1}{2}\sum_{i=1}^{M} f_c(X_i)\right]. \tag{5}$$

In SBL, the sparsity of parameter X is controlled by a regularization function $f_c(\cdot)$, which is generally formulated as a non-decreasing concave function to enhance sparsity by penalizing small coefficients less than large ones. Each $f_c(X_i)$ corresponds to the negative log prior to each component, i.e., $P(X_i) \propto \exp\left(-\frac{1}{2}f_c(X_i)\right)$. Therefore, the prior $P(X)$ is constructed as a product of independent priors over each X_i. Given an assumed prior distribution $P(X) = \prod_{i=1}^{M} P(X_i)$, the posterior distribution of X can be derived via Bayes' theorem as follows:

$$P(X|\Phi) = \frac{P(\Phi|X)P(X)}{\int P(\Phi|X)P(X)\mathrm{d}X}. \tag{6}$$

Due to model uncertainty and complex prior distributions, the posterior distribution $P(X|\Phi)$ is typically non-Gaussian, making the problem more difficult to solve. To address this challenge, it is approximated by a Gaussian distribution. Here, $\gamma \in \mathcal{R}_+^{\mathcal{M}}$ denotes the hyperparameter vector controlling the prior variance of each X_i. By estimating an optimal $\hat{\gamma}$, the approximated posterior $P(X|\Phi, \hat{\gamma})$ remains computationally efficient while closely matching the true posterior $P(X|\Phi)$. The inference process proceeds as follows:

$$\min_{\gamma \geq 0, X} \|AX - \Phi\|_2^2 + \log\left|\lambda I + A\Gamma A^T\right| + \lambda X^T \Gamma^{-1} X, \tag{7}$$

where $\Gamma = \mathrm{diag}[\gamma]$ is a diagonal matrix representing the prior covariance of the parameters. It is evident that directly estimating the model coefficients γ and X from Eq. (7) is challenging. To address this, we reformulate Eq. (7) as follows:

$$\min_{\gamma \geq 0, X} g(X, \gamma) - h(\gamma), \tag{8}$$

where $g(X, \gamma) = ||AX - \Phi||_2^2 + \lambda \sum_k \frac{X_k^2}{\gamma_i}$ and $h(\gamma) = \log|\lambda I + P\Gamma P^T|$. Since $h(\gamma)$ is convex and differentiable, its gradient can be directly computed. The model parameter $\hat{X}_{k+1}$ and the hyperparameter $\hat{\gamma}_{k+1}$ are updated using the following iterative strategy:

$$\left[\hat{X}_{k+1}, \hat{\gamma}_{k+1}\right] = \arg\min_{\gamma \geq 0, X} g(X, \gamma) - \nabla_\gamma h\left(\hat{\gamma}_k\right)^T \gamma. \tag{9}$$

Based on the definition of $h(\gamma)$, its negative gradient is as follows:

$$-\nabla_\gamma h(\hat{\gamma}_k)^T \& = \mathrm{diag}\left[A^T(\lambda I + A\Gamma_k A^T)^{-1} A\right]. \tag{10}$$

Let $\alpha_k = \mathrm{diag}[A^T(\lambda I + A\Gamma_k A^T)^{-1} A]$ for notation simplicity. Then, Eq. (9) becomes

$$\left[\hat{X}_{k+1}, \hat{\gamma}_{k+1}\right] = \arg\min_{\gamma \geq 0, X} \|AX - \Phi\|_2^2 + \lambda \sum_j \left(\frac{X_j^2}{\gamma_j} + (\alpha_k)_j \gamma_j\right), \tag{11}$$

where $(\alpha_k)_j$ denotes the jth diagonal element of α_k. Since Eq. (11) is convex in X and γ, global minimization can be achieved by first solving for γ with fixed X. The update of γ is expressed as

$$\hat{\gamma}_{k+1} = \arg\min_{\gamma \geq 0} \|AX - \Phi\|_2^2 + \lambda \sum_j \left(\frac{X_j^2}{\gamma_j} + (\alpha_k)_j \gamma_j\right), \tag{12}$$

where $(\hat{\gamma}_{k+1})_j = |X_j|/\sqrt{(\alpha_k)_j}$. Substituting the updated $\hat{\gamma}_{k+1}$ into Eq. (11) yields X, enabling iterative convergence to the global optimum:

$$\hat{X}_{k+1} = \arg\min_X \|AX - \Phi\|_2^2 + 2\lambda\Sigma\sqrt{(\alpha_k)_j}\,|X_j|. \tag{13}$$

Equation (13) can be further reduced to the classical weighted L_1 minimization problem as follows:

$$\hat{X}_{k+1} = \arg\min_X \frac{1}{2}\|AX - \Phi\|_2^2 + \lambda\|GX\|_1, \quad (14)$$

where $G = \mathrm{diag}[w_k]$ is a diagonal matrix with adaptive weights w_k. These weights are dynamically adjusted through the iterative update of hyperparameters to promote sparsity and are computed as $w_k = \sqrt{(\alpha_k)}$, where α_k is derived from the parameter matrix at the kth iteration. Then α_{k+1} is calculated as

$$\alpha_{k+1} = \mathrm{diag}\left[A^T(\lambda I + A\Gamma_{k+1}A^T)^{-1}A\right], \quad (15)$$

where $\Gamma_{k+1} = \mathrm{diag}[(\gamma_{k+1})_1, (\gamma_{k+1})_2, \ldots, (\gamma_{k+1})_M]$.

The computation of $\hat{\gamma}_{k+1}$ is given as follows:

$$(\hat{\gamma}_{k+1})_i = |(\hat{X}_{k+1})_i|/\sqrt{(\alpha_k)_i}. \quad (16)$$

Based on the above formulation, the weight matrix G is calculated to adaptively control the regularization strength, balancing data fidelity and prior constraints throughout the iterative process.

2. Augmented Lagrangian Algorithm

In FMT reconstruction, the weighted L_1 minimization problem in Eq. (14) enforces sparsity to improve the stability of solving the ill-posed inverse problem. It can be reformulated as the following constrained optimization problem:

$$\min_{X, v\in R^M} f_1(v) + f_2(X) \quad \text{s.t. } v = GX, \quad (17)$$

where $f_1(v) = \lambda||v||_1$ denotes the sparsity-promoting regularization term, while $f_2(X) = \frac{1}{2}||AX - \Phi||_2^2$ represents the data fidelity term. The constraint in Eq. (17), $||v - GX||_2^2 = 0$, implies $v = GX$ must be strictly satisfied at the optimal solution. The optimization problem can thus be reformulated as a quadratically constrained optimization problem:

$$\min_{X, v\in R^M} f_1(v) + f_2(X) + \frac{\mu}{2}\|GX - v\|_2^2 \text{ s.t.v} - GX = 0, \quad (18)$$

where μ denotes the Lagrange multiplier that enforces constraints, enabling Eq. (18) to better approximate the global optimum of the weighted L_1 minimization problem. Using the AL optimization framework, Eq. (18) is reformulated as

$$L_\mu(v, X, u) = f_1(v) + f_2(X) - u^T(GX - v) + \frac{\mu}{2}||GX - v||_2^2, \quad (19)$$

where u is the dual variable used to impose a penalty on the constraint. Equation (19) is solved by alternately updating X, v, and u while keeping the others fixed. This alternating optimization strategy decomposes the problem into simpler sub-problems, improving computational efficiency and convergence.

When $v = GX$, Eq. (19) reduces to the weighted L_1 minimization problem. Given u, v, and G, X can be directly obtained. The weighting matrix G is then updated using Eqs. (15) and (16), enabling the model to dynamically reflect the sparsity structure and data variation. The updated G is expressed as

$$G = \mathrm{diag}\left[\sqrt{\alpha_{k+1}}\right]. \quad (20)$$

By substituting u with d in Eq. (18), the problem becomes

$$L_\mu(v, X, d) = f_1(v) + f_2(X) + \frac{\mu}{2}||GX - v - d||_2^2. \quad (21)$$

The solution X is obtained by iteratively solving the following convex sub-problems:

$$\begin{cases} \hat{X}_{k+1} = \arg\min_X f_2(X) + \frac{\mu}{2}\|GX - v_k - d_k\|_2^2 \\ v_{k+1} = \arg\min_v f_1(v) + \frac{\mu}{2}\|G\hat{X}_{k+1} - v - d_k\|_2^2 \\ d_{k+1} = d_k - \left(G\hat{X}_{k+1} - v_{k+1}\right) \end{cases}. \quad (22)$$

In the Bayesian framework, the weighting matrix G is initialized as a diagonal identity matrix and updated iteratively using Eq. (20). For the first two sub-problems in Eq. (22), a gradient-based method is employed. The first-order derivative of the objective function is set to zero to derive the corresponding equation:

$$\begin{cases} X_{k+1} = \left(A^TA + \mu G^TG\right)^{-1}\left(A^T\Phi + \mu G^T(v_k + d_k)\right) \\ v_{k+1} = \mathrm{sign}\left(GX_{k+1} - d_k\right)\cdot\max\left(|GX_{k+1} - d_k| - \frac{\lambda}{\mu}, 0\right) \\ d_{k+1} = d_k - (GX_{k+1} - v_{k+1}) \end{cases}. \quad (23)$$

To enhance solution accuracy, the regularization parameter λ is adaptively updated based on the modeling error. The modeling error at iteration $k+1$ is defined as

$$\mathrm{Err}_{k+1} = \frac{1}{2}\left|\left|\Phi - A\hat{X}_{k+1}\right|\right|_2^2. \quad (24)$$

The modeling error ratio is defined as $\beta_{k+1} = |\mathrm{Err}_{k+1}/\mathrm{Err}_k - 1|$ to quantify the relative change in error between iterations. The ratio is utilized to adaptively adjust the regularization parameter λ, enhancing the reconstruction performance. The update rule is expressed as

$$\lambda_{k+1} = \begin{cases} 0.9\,\lambda_k & \text{if } \beta_{k+1} > 0.15 \\ 1.1\,\lambda_k & \text{otherwise} \end{cases}. \quad (25)$$

In conclusion, the main procedure of the ABAL algorithm is outlined in Algorithm 1.

3. EXPERIMENT DESIGN

In this section, numerical simulation and *in vivo* mouse experiments with implanted light sources were conducted. Three existing algorithms: FISTA-L_1, IVTCG-L_1, and OMP-L_0 were used for comparison in terms of location accuracy, morphological recovery, and robustness. All experiments and procedures were conducted on a laptop equipped with an AMD Ryzen 7 3700U processor (2.30 GHz), Radeon Vega Mobile Graphics, and 8 GB of RAM.

A. Evaluation Index

Two evaluation metrics were adopted: localization error (LE) [40] and the Dice coefficient (DICE) [41]. LE is defined as the

Algorithm 1. ABAL algorithm for FMT reconstruction

Input: the detected surface photon measurement $\Phi \epsilon \mathbb{R}^{m\times 1}$, the system matrix $A \epsilon \mathbb{R}^{m\times n}$, the regularization parameters λ_0.
Parameter initialization: the initial optimal approximation solution $\hat{X}_0 = \mathbf{0}$, the maximum iteration number $maxIter = 100$, the weight matrix $G = \mathbf{I}$, $v_0 = d_0 = \mathbf{0}$, $\mu = \lambda_0$, the current iteration $k = 0$, $tol = 1e-6$.
While $||X^k - X^{k-1}||_2 > tol$ or $k < maxIter$ do
1: Update X, v, and d:

$$X_{k+1} = (A^T A + \mu G^T G)^{-1}(A^T \Phi + \mu G^T (v_k + d_k))$$
$$v_{k+1} = sign(GX_{k+1} - d_k) \cdot max\left(|GX_{k+1} - d_k| - \tfrac{\lambda}{\mu}, 0\right)$$
$$d_{k+1} = d_k - (GX_{k+1} - v_{k+1})$$

2: Update weighting matrix G:

$$\alpha_{k+1} = diag\left[A^T(\lambda I + A\Gamma_{k+1}A^T)^{-1}A\right]$$

3: $Err_{k+1} = \frac{1}{2}||\Phi - A\hat{X}_{k+1}||_2^2$

4: $\lambda_{k+1} = \begin{cases} 0.9\,\lambda_k & if\beta_{k+1} > 0.15 \\ 1.1\,\lambda_k & otherwise \end{cases}$

5: $k = k + 1$
End while
Output: $\hat{X}$

Euclidean distance between the center of the reconstructed target (x_r, y_r, z_r) and the center of the true target (x_t, y_t, z_t). A lower LE value indicates higher positioning accuracy of the reconstructed result

$$\mathrm{LE} = \sqrt{(x_r - x_t)^2 + (y_r - y_t)^2 + (z_r - z_t)^2}. \quad (26)$$

DICE is used to evaluate the spatial overlap between the reconstructed region R_r and the true region R_t. It is defined as

$$\mathrm{DICE} = 2\frac{|R_r \cap R_t|}{|R_r| + |R_t|}. \quad (27)$$

The DICE value ranges from 0 to 1. A higher DICE value indicates greater similarity between the reconstructed region and the true region, reflecting better morphological recovery.

Table 1. Optical Parameters of the Heterogeneous Cylindrical Phantom at 650 nm

Tissue	$\mu_a(r)(\mathrm{mm}^{-1})$	$\mu_s(r)(\mathrm{mm}^{-1})$	g
Muscle	0.0052	10.80	0.900
Bone	0.0060	60.09	0.900
Heart	0.0083	6.733	0.850
Liver	0.0329	7.000	0.900
Lung	0.0133	19.70	0.900

B. Numerical Simulation Experimental Setup

A heterogeneous cylindrical phantom with a radius of 10 mm and a height of 30 mm was constructed to simulate biological tissue. The model includes five major organs: muscle, bone, heart, liver, and lungs. The optical parameters at a wavelength of 650 nm are listed in Table 1 [42]. The model was discretized into a tetrahedral mesh with 4626 nodes and 25,840 elements using COMSOL Multiphysics 5.6 (COMSOL, Inc., Burlington, Massachusetts) [43], as shown in Fig. 1(a). The single-source target position is illustrated in Fig. 1(b). The forward simulation result of the single-source experiment was obtained using the Monte Carlo (MC) method implemented in the molecular optical simulation environment (MOSE, Version 2.3) software [44], as shown in Fig. 1(c).

Three experiments were designed: a single-source simulation with a 1 mm radius source centered at (−5, −4, 11) mm; a dual-source simulation with two identical sources at (−2, 2, 4) mm and (−2, 2, 23) mm; and an anti-noise experiment in which Gaussian noise with intensity levels ranging from 5% to 25% (in 5% increments) was added to the single-source simulation to evaluate the robustness of the proposed method.

C. Light Source Implantation Experimental Setup

To evaluate the feasibility of the ABAL method for *in vivo* FMT reconstruction, a light source implantation experiment was performed on a female BALB/c nude mouse (6–8 weeks old) using a dual-modality FMT/CT imaging system, as shown in Fig. 2. Specifically, a spherical fluorescent bead with a radius of 1 mm containing Cy5.5 solution (about 20 μl) was implanted

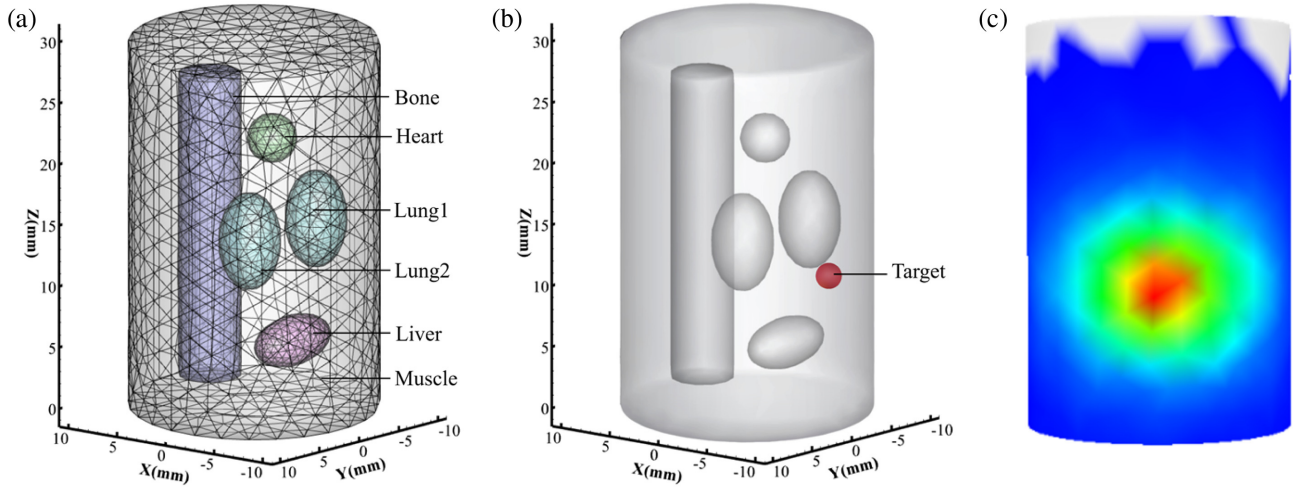

Fig. 1. Heterogeneous cylindrical phantom for numerical simulation studies. (a) The 3D view of the tetrahedral mesh. (b) The cylindrical phantom with single source. (c) The forward simulation result of cylindrical phantom with single source.

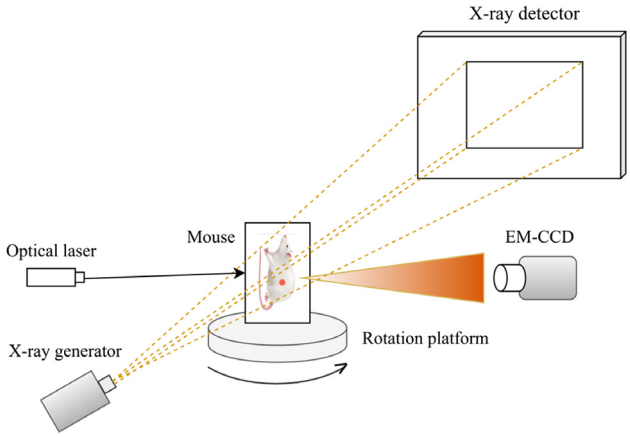

Fig. 2. The schematic diagram of the FMT/CT system.

into the abdominal cavity of the mouse at (14.5, 8, 16.6) mm to simulate a fluorescence target. The bead was encapsulated in a plastic material to enable precise localization by CT imaging. The mouse was anesthetized with a 3% isoflurane-air mixture and fixed vertically on a motorized rotation stage to minimize motion artifacts. Six hours after implantation, a 750 nm continuous-wave laser was used for excitation. The fluorescence signal was collected by a thermoelectrically cooled electron multiplying charge coupled device (EMCCD) camera (iXonEM +888, −80°C) with a 120° field of view and a 1 s exposure time. A 750 ± 10 nm bandpass filter was applied to enhance contrast and suppress background noise. Subsequently, CT scanning was performed to acquire anatomical data. A landmark-based rigid registration method was employed to align the fluorescence and CT images. The 2D irradiance distribution was projected onto the 3D surface of the mouse model. Major organs including muscle, heart, lungs, liver, stomach, and kidneys were segmented using Amira 5.2 (Visage Imaging, Australia). The mouse model was discretized into 6639 nodes and 30,279 tetrahedral elements for 3D reconstruction.

4. RESULTS

A. Numerical Simulations Results

1. Single-Source Experiment

The reconstruction results of the single-source experiment are shown in Fig. 3. The left subfigure displays the 3D reconstructed results of FISTA-L_1, IVTCG-L_1, OMP-L_0, and ABAL, where the reconstructed fluorescence source is depicted in red. The right subfigure shows the cross-sectional view at the $X = -5$ mm plane, with the red area representing the reconstructed source and the white circle denoting the actual location and boundary of the true target. The quantitative evaluation results of the four methods are summarized in Table 2. It can be seen that the ABAL method achieves the lowest LE (0.258 mm) and the highest DICE (0.783), indicating better positioning accuracy and morphological recovery compared to the other three methods.

2. Dual-Source Experiment

The reconstruction results of the dual-source experiment are shown in Fig. 4. The left subfigure displays the 3D

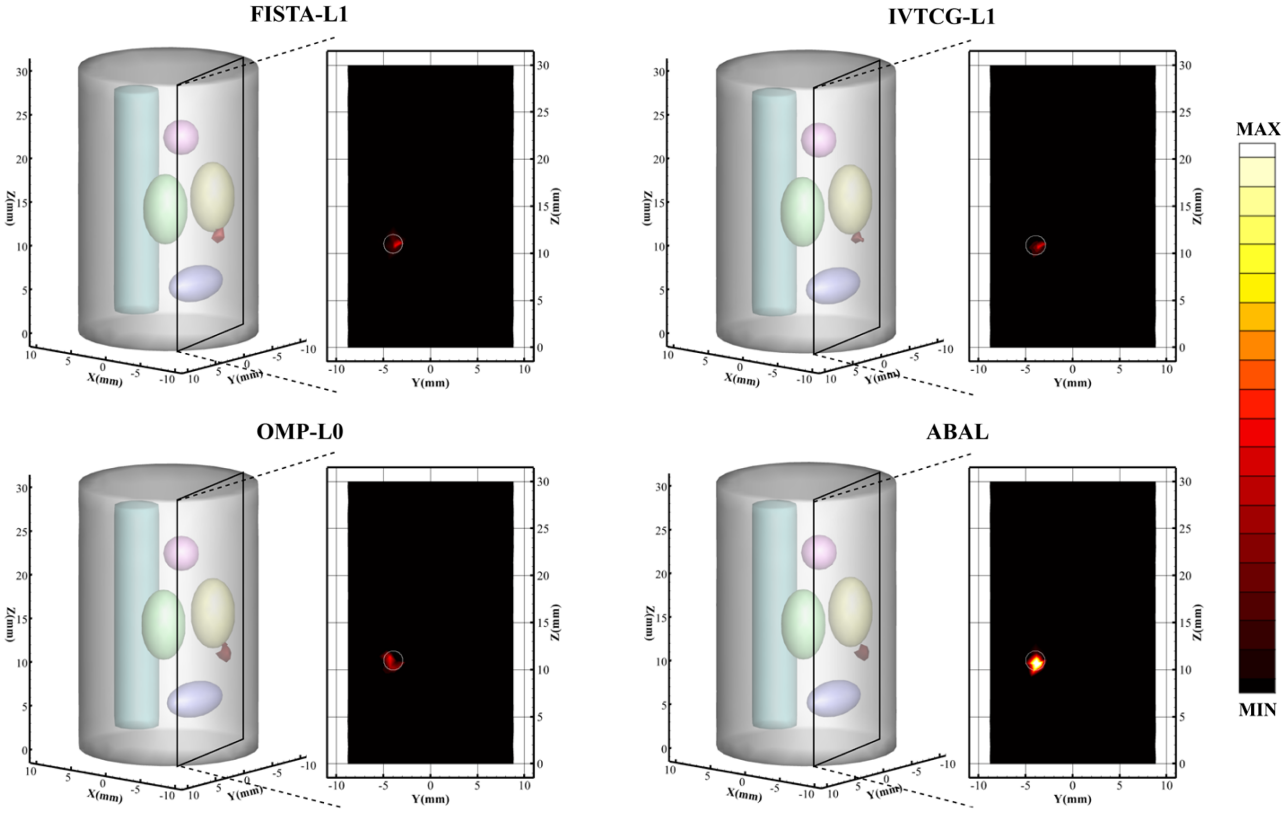

Fig. 3. Reconstruction results of four methods for a single spherical target.

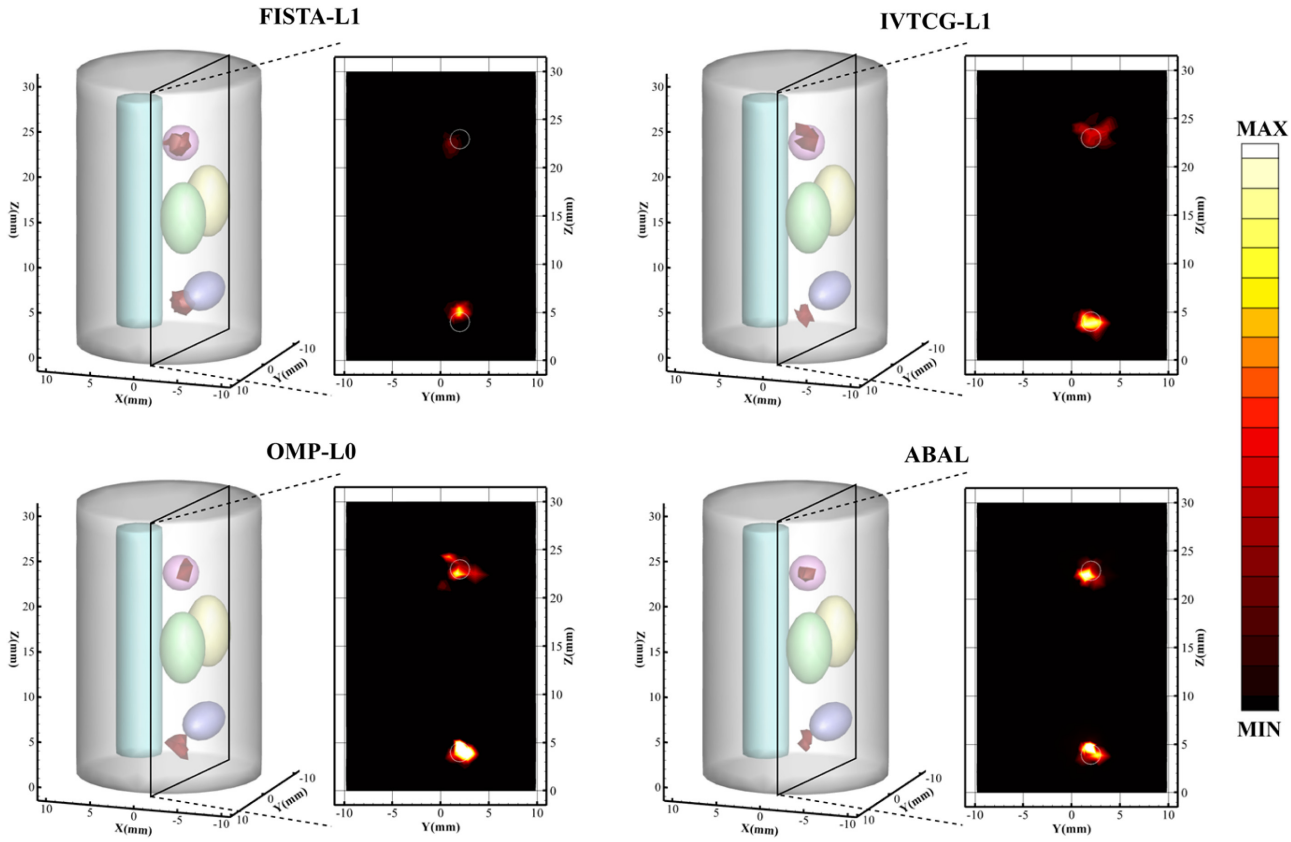

Fig. 4. Reconstruction results of four methods for dual source.

Table 2. Quantitative Results of Different Methods in Single-Source Experiment

Method	Reconstructed Results (mm)	LE (mm)	DICE
FISTA-L_1	(−4.260, −3.665, 11.167)	0.829	0.422
IVTCG-L_1	(−4.449, −3.698, 10.909)	0.635	0.563
OMP-L_0	(−4.667, −4.054, 10.883)	0.358	0.554
ABAL	(−4.902, −3.821, 10.843)	0.258	0.783

reconstruction results of FISTA-L_1, IVTCG-L_1, OMP-L_0, and ABAL. The right subfigure shows the cross-sectional view at the $X = -2.0$ mm plane. In these images, the reconstructed sources are shown in red, and the actual source positions are marked with white circles, consistent with the single-source experiment. The quantitative evaluation results of the four methods are summarized in Table 3. It can be seen that the ABAL method achieves the lowest LE (0.459 and 0.506 mm) and the highest DICE (0.726 and 0.792), indicating better positioning accuracy and morphological recovery compared to the other methods.

3. Anti-Noise Experiment

The results of the anti-noise experiment are presented in Fig. 5. Gaussian noise at levels of 5%, 10%, 15%, 20%, and 25% was added to the measurement data based on the single-source experiment. It can be seen that at lower noise levels (5% and 10%), LE increases slightly and DICE decreases marginally. As the noise level rises to 15%–25%, LE exhibits minor fluctuations and DICE gradually decreases but remains above 0.65. These results demonstrate that the ABAL method achieves robust reconstruction performance under varying noise conditions.

Table 3. Quantitative Results of Different Methods in Dual-Source Experiment

Method	Reconstructed Results (mm)	LE (mm)	DICE
FISTA-L_1	(−2.071, 2.065, 4.694)	0.701	0.336
	(−1.261, 1.554, 22.226)	1.159	0.381
IVTCG-L_1	(−1.690, 1.799, 3.892)	0.385	0.757
	(−2.432, 2.658, 23.517)	0.942	0.394
OMP-L_0	(−2.229, 2.432, 3.752)	0.548	0.657
	(−2.221, 2.269, 22.520)	0.593	0.392
ABAL	(−1.948, 2.064, 4.452)	0.459	0.726
	(−2.189, 1.818, 22.567)	0.506	0.792

B. Light Source Implantation Experiment Results

The results of the light source implantation experiment are shown in Fig. 6, which presents the reconstruction results of four methods: FISTA-L_1, IVTCG-L_1, OMP-L_0, and ABAL. For each method, three views are displayed: the 3D reconstruction view, the axial view at plane $Z = 16.6$ mm, and the sagittal view at plane $X = 14.5$ mm. In the sectional views, the reconstructed fluorescence source is shown in red, while the actual position and boundary of the implanted fluorescent microsphere are indicated by a white circle. As observed from

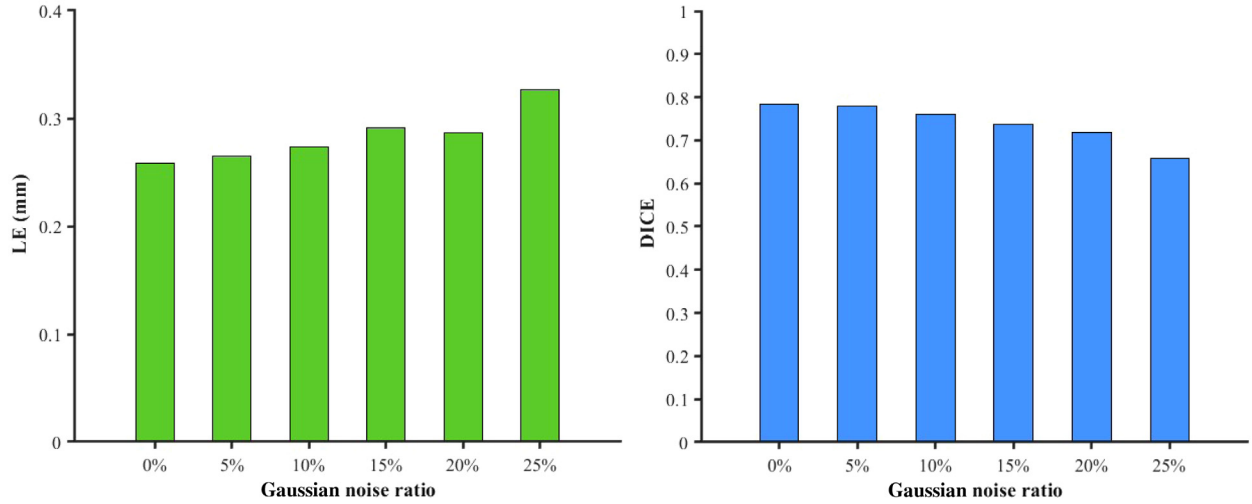

Fig. 5. Illustration of LE and DICE at different noise levels.

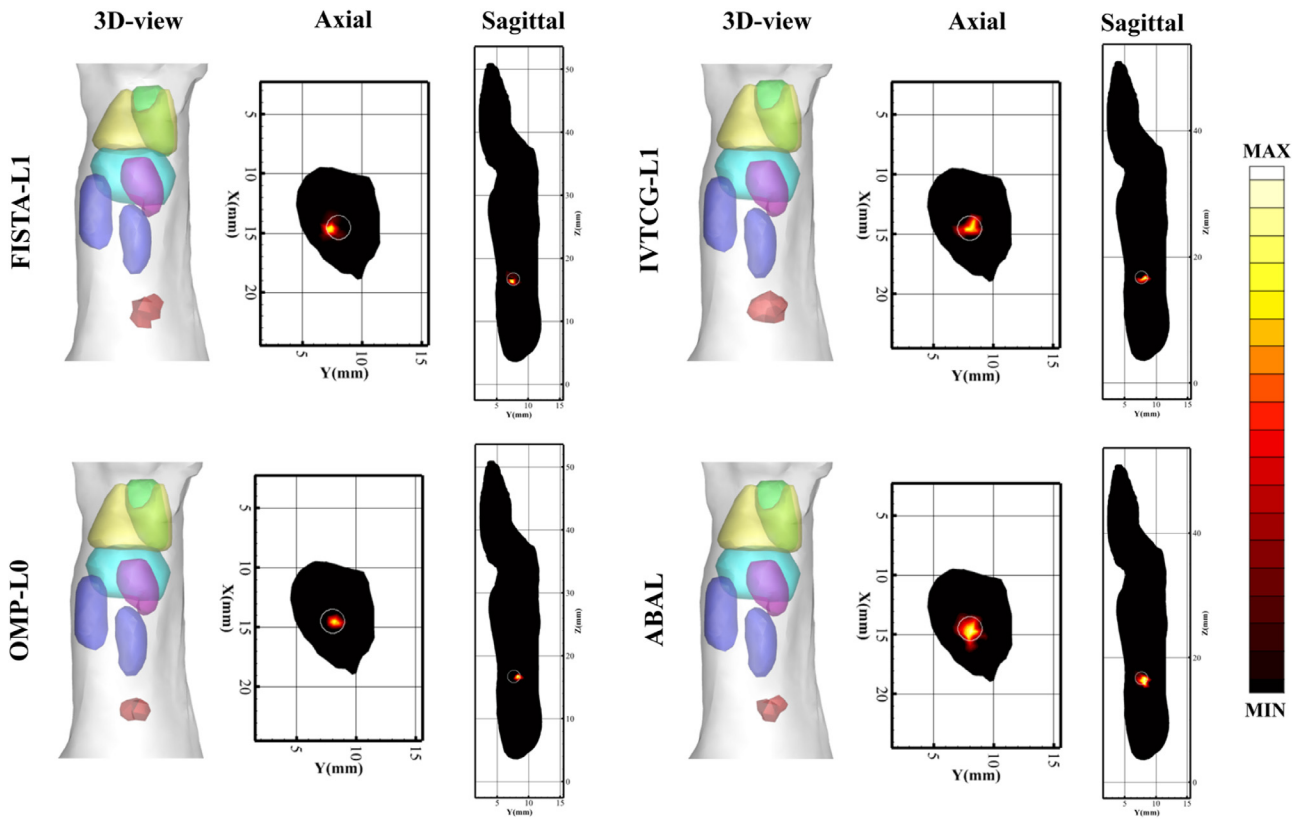

Fig. 6. The reconstruction results of the light source implantation experiment.

both 3D and sectional views, the ABAL method demonstrates better spatial alignment with the true target compared to the other methods. For quantitative analysis, the LE and DICE values of the four methods are summarized in Table 4. The ABAL method yields the lowest LE (0.208 mm) and the highest DICE (0.800), indicating superior performance in both localization accuracy and morphological recovery.

Table 4. Quantitative Results of Light Source Implantation Experiment

Method	Reconstructed Results (mm)	LE (mm)	DICE
FISTA-L_1	(14.723, 7.413, 16.593)	0.628	0.444
IVTCG-L_1	(14.190, 8.318, 16.684)	0.453	0.667
OMP-L_0	(14.648, 8.031, 16.240)	0.391	0.500
ABAL	(14.504, 8.153, 16.743)	0.208	0.800

5. DISCUSSION AND CONCLUSION

FMT is a promising imaging modality with high sensitivity, non-invasiveness, and quantitative capability, enabling precise localization of fluorescence-labeled molecular probes *in vivo*. Nevertheless, the complex light scattering and absorption of photons in biological tissues make the FMT reconstruction

problem highly ill-posed, which poses significant challenges in achieving accurate and robust reconstructions, especially in multiple-source and complex morphologies.

To address these issues, this study proposed an adaptive reconstruction algorithm named ABAL, which combines the sparsity-promoting SBL with an efficient AL optimization strategy. SBL adaptively adjusts regularization weights based on reconstruction feedback, enhancing the flexibility and sparsity of the solution. Meanwhile, AL optimization decomposes the original non-convex problem into convex sub-problems, accelerating convergence and reducing computational complexity. This integration improves both localization accuracy and morphological recovery in FMT.

The performance of ABAL was systematically validated through numerical simulations and light source implantation experiments. Compared with conventional methods including FISTA-L_1, IVTCG-L_1, and OMP-L_0, ABAL consistently achieved better reconstruction results in terms of LE and DICE. The light source implantation experiment further confirmed its practical feasibility, with ABAL achieving an LE of 0.208 mm and a DICE of 0.800, indicating high consistency between the reconstructed and actual source distributions.

Although the proposed method has shown promising performance, certain limitations remain. The reconstruction quality may be affected by photon shot noise, finite-element mesh resolution, and anatomical heterogeneity within complex biological tissues. Future efforts may focus on enhancing automation and computational efficiency through adaptive mesh refinement, GPU-based parallel reconstruction, and the integration of anatomical priors.

In summary, ABAL provides an effective solution for FMT reconstruction by combining adaptive regularization and efficient optimization. Its superior performance in terms of localization accuracy, robustness, and morphological recovery highlights its potential for preclinical imaging and biomedical applications.

Funding. National Major Scientific Research Instrument Development Projects of China (82127805); Key Research and Development Program of Shaanxi Province (2024SF-YBXM-681); National Natural Science Foundation of China (61701403, 61806164).

Disclosures. The authors declare no conflicts of interest.

Data availability. Data underlying the results presented in this paper are not publicly available at this time but may be obtained from the authors upon reasonable request.

REFERENCES

1. P. Zhang, G. Fan, T. Xing, *et al.*, "UHR-DeepFMT: ultra-high spatial resolution reconstruction of fluorescence molecular tomography based on 3-D fusion dual-sampling deep neural network," IEEE Trans. Med. Imaging **40**, 3217–3228 (2021).
2. H. Meng, K. Wang, Y. Gao, *et al.*, "Adaptive Gaussian weighted Laplace prior regularization enables accurate morphological reconstruction in fluorescence molecular tomography," IEEE Trans. Med. Imaging **38**, 2726–2734 (2019).
3. F. Stuker, C. Baltes, K. Dikaiou, *et al.*, "Hybrid small animal imaging system combining magnetic resonance imaging with fluorescence tomography using single photon avalanche diode detectors," IEEE Trans. Med. Imaging **30**, 1265–1273 (2011).
4. D. Han, J. Tian, S. Zhu, *et al.*, "A fast reconstruction algorithm for fluorescence molecular tomography with sparsity regularization," Opt. Express **18**, 8630–8646 (2010).
5. S. Jiang, J. Liu, Y. An, *et al.*, "Novel 1,2 l-norm optimization method for fluorescence molecular tomography reconstruction," Biomed. Opt. Express **7**, 2342–2359 (2016).
6. C. Cao, Z. Jin, X. Shi, *et al.*, "First clinical investigation of near-infrared window IIa/IIb fluorescence imaging for precise surgical resection of gliomas," IEEE Trans. Biomed. Eng. **69**, 2404–2413 (2022).
7. X. Shi, Z. Zhang, Z. Zhang, *et al.*, "Near-infrared window II fluorescence image-guided surgery of high-grade gliomas prolongs the progression-free survival of patients," IEEE Trans. Biomed. Eng. **69**, 1889–1900 (2021).
8. L. Kong, Y. An, Q. Liang, *et al.*, "Reconstruction for fluorescence molecular tomography via adaptive group orthogonal matching pursuit," IEEE Trans. Biomed. Eng. **67**, 2518–2529 (2020).
9. X. Song, D. Wang, N. Chen, *et al.*, "Reconstruction for free-space fluorescence tomography using a novel hybrid adaptive finite element algorithm," Opt. Express **15**, 18300–18317 (2007).
10. J. Shi, B. Zhang, F. Liu, *et al.*, "Efficient L1 regularization-based reconstruction for fluorescent molecular tomography using restarted nonlinear conjugate gradient," Opt. Lett. **38**, 3696–3699 (2013).
11. H. Liu, X. Yang, T. Song, *et al.*, "Multispectral hybrid Cerenkov luminescence tomography based on the finite element SPn method," J. Biomed. Opt. **20**, 086007 (2015).
12. E. Edjlali and Y. Bérubé-Lauzière, "L_q–L_p optimization for multigrid fluorescence tomography of small animals using simplified spherical harmonics," J. Quant. Spectrosc. Radiat. Transf. **205**, 163–173 (2018).
13. N. Cao, A. Nehorai, and M. Jacob, "Image reconstruction for diffuse optical tomography using sparsity regularization and expectation-maximization algorithm," Opt. Express **15**, 13695–13708 (2007).
14. H. Chen, K. Shou, S. Chen, *et al.*, "Smart self-assembly amphiphilic cyclopeptide-dye for near-infrared window-II imaging," Adv. Mater. **33**, 2006902 (2021).
15. W. Bangerth, "A framework for the adaptive finite element solution of large-scale inverse problems," SIAM J. Sci. Comput. **30**, 2965–2989 (2008).
16. Y. An, J. Liu, G. Zhang, *et al.*, "A novel region reconstruction method for fluorescence molecular tomography," IEEE Trans. Biomed. Eng. **62**, 1818–1826 (2015).
17. Z. Hu, M. Zhao, Y. Qu, *et al.*, "In vivo 3-dimensional radiopharmaceutical-excited fluorescence tomography," J. Nucl. Med. **58**, 169–174 (2017).
18. J. Fan and R. Li, "Variable selection via nonconcave penalized likelihood and its oracle properties," J. Am. Stat. Assoc. **96**, 1348–1360 (2001).
19. C. H. Zhang, "Nearly unbiased variable selection under minimax concave penalty," Ann. Stat. **38**, 894–942 (2010).
20. C. Olsson, M. Carlsson, F. Andersson, *et al.*, "Non-convex rank/sparsity regularization and local minima," in *Proceedings of the IEEE International Conference on Computer Vision* (2017), pp. 332–340.
21. F. Wen, L. Chu, P. Liu, *et al.*, "A survey on nonconvex regularization-based sparse and low-rank recovery in signal processing, statistics, and machine learning," IEEE Access **6**, 69883 (2018).
22. Z. Li, C. Wan, B. Tan, *et al.*, "A fast DC-based dictionary learning algorithm with the SCAD penalty," Neurocomputing **429**, 89–100 (2021).
23. L. Su, H. Gao, L. Chen, *et al.*, "ROMP-DCP: Dictionary learning via regularized orthogonal matching pursuit and difference of convex programming for robust fluorescence molecular tomography," Biomed. Signal Process. Control **102**, 107327 (2025).
24. J. Feng, K. Jia, C. Qin, *et al.*, "Three-dimensional bioluminescence tomography based on Bayesian approach," Opt. Express **17**, 16834–16848 (2009).
25. F. Orieux, E. Sepulveda, V. Loriette, *et al.*, "Bayesian estimation for optimized structured illumination microscopy," IEEE Trans. Image Process. **21**, 601–614 (2011).
26. Y. Mishchencko, J. T. Vogelstein, and L. Paninski, "A Bayesian approach for inferring neuronal connectivity from calcium fluorescent imaging data," Ann. Appl. Stat. **5**, 1229–1261 (2011).

27. M. E. Tipping, "Sparse Bayesian learning and the relevance vector machine," J. Mach. Learn. Res. **1**, 211–244 (2001).
28. S. Zhang, Y. Liu, X. Li, *et al.*, "Variational Bayesian sparse signal recovery with LSM prior," IEEE Access **5**, 26690–26702 (2017).
29. A. Durmus, E. Moulines, and M. Pereyra, "Efficient Bayesian computation by proximal Markov chain Monte Carlo: when Langevin meets Moreau," SIAM J. Imag. Sci. **11**, 473–506 (2018).
30. J. M. Bardsley, "MCMC-based image reconstruction with uncertainty quantification," SIAM J. Sci. Comput. **34**, A1316–A1332 (2012).
31. A. Beck and M. Teboulle, "A fast iterative shrinkage-thresholding algorithm for linear inverse problems," SIAM J. Imag. Sci. **2**, 183–202 (2009).
32. X. He, J. Liang, X. Wang, *et al.*, "Sparse reconstruction for quantitative bioluminescence tomography based on the incomplete variables truncated conjugate gradient method," Opt. Express **18**, 24825–24841 (2010).
33. J. Wang and B. Shim, "On the recovery limit of sparse signals using orthogonal matching pursuit," IEEE Trans. Signal Process. **60**, 4973–4976 (2012).
34. C. Li, G. S. Mitchell, and S. R. Cherry, "Cerenkov luminescence tomography for small-animal imaging," Opt. Lett. **35**, 1109–1111 (2010).
35. Q. Zhang, H. Zhao, D. Chen, *et al.*, "Source sparsity based primal-dual interior-point method for three-dimensional bioluminescence tomography," Opt. Commun. **284**, 5871–5876 (2011).
36. J. H. Lee, A. Joshi, and E. M. Sevick-Muraca, "Fully adaptive finite element based tomography using tetrahedral dual-meshing for fluorescence enhanced optical imaging in tissue," Opt. Express **15**, 6955–6975 (2007).
37. A. Joshi, W. Bangerth, and E. M. Sevick-Muraca, "Adaptive finite element based tomography for fluorescence optical imaging in tissue," Opt. Express **12**, 5402–5417 (2004).
38. G. Gasso, A. Rakotomamonjy, and S. Canu, "Recovering sparse signals with a certain family of nonconvex penalties and DC programming," IEEE Trans. Signal Process. **57**, 4686–4698 (2009).
39. X. Tang, L. Zhang, and X. Li, "Bayesian augmented Lagrangian algorithm for system identification," Syst. Control Lett. **120**, 9–16 (2018).
40. H. Guo, L. Gao, J. Yu, *et al.*, "Sparse-graph manifold learning method for bioluminescence tomography," J. Biophotonics **13**, e201960218 (2020).
41. L. Yin, K. Wang, T. Tong, *et al.*, "Adaptive grouping block sparse Bayesian learning method for accurate and robust reconstruction in bioluminescence tomography," IEEE Trans. Biomed. Eng. **68**, 3388–3398 (2021).
42. Y. Hou, X. Hua, C. Xin, *et al.*, "Single-view enhanced Cerenkov luminescence tomography based on sparse Bayesian learning," Acta Opt. Sin. **37**, 298–308 (2017).
43. B. Parvitte, C. Risser, R. Vallon, *et al.*, "Quantitative simulation of photoacoustic signals using finite element modelling software," Appl. Phys. B **111**, 383–389 (2013).
44. N. Ren, J. Liang, X. Qu, *et al.*, "GPU-based Monte Carlo simulation for light propagation in complex heterogeneous tissues," Opt. Express **18**, 6811–6823 (2010).